

1 Application of fractal models to delineate mineralized zones in  
2 the Pulang porphyry copper deposit, Yunnan, Southwest China

3 Xiaochen Wang<sup>a</sup>, Qinglin Xia<sup>a,b,\*</sup>, Tongfei Li<sup>a</sup>, Shuai Leng<sup>a</sup>, Yanling Li<sup>a</sup>, Li  
4 Kang<sup>a</sup>, Zhijun Chen<sup>a</sup>, Lianrong Wu<sup>c</sup>

5 <sup>a</sup> Faculty of Earth Resources, China University of Geosciences, Wuhan 430074, China

6 <sup>b</sup> Collaborative Innovation Center for Exploration of Strategic Mineral Resources,  
7 Wuhan 430074, China

8 <sup>c</sup> Yunnan Diqing Nonferrous Metal Co., Ltd., Shangri-La 674400, China

9 **Abstract**

10 The aim of this study is to delineate and recognize various mineralized zones and  
11 barren host rocks based on the surface and subsurface lithochemical data utilizing  
12 the number-size (N-S), concentration-volume (C-V) and power spectrum-volume (S-V)  
13 fractal models in the Pulang porphyry copper deposit, southwest China. The N-S  
14 model reveals three mineralized zones characterized by Cu thresholds of 0.28% and  
15 1.45%, with zones <0.28% Cu representing weakly mineralized zones and barren host  
16 rocks, with zones 0.28%-1.45% Cu representing moderately mineralized zones and  
17 zones >1.45% Cu representing highly mineralized zones. Results obtained by the C-V  
18 model depict four geochemical zones defined by Cu thresholds of 0.25%, 1.48% and  
19 1.88%, which represent non-mineralized wall rocks (Cu<0.25%), weakly mineralized  
20 zones (0.25%-1.48%), moderately mineralized zones (1.48%-1.88%), and highly  
21 mineralized zones (Cu>1.88%). S-V model is used by performing 3D fast Fourier  
22 transformation on assay data in the frequency domain. The S-V model reveals three  
23 mineralized zones characterized by Cu thresholds of 0.23% and 1.33%, with zones of  
24 <0.23% Cu representing leached zone and barren host rocks, with zones of 0.23%-1.33%  
25 Cu representing the hypogene zones and zones of >1.33% Cu representing supergene  
26 enrichment zones. All the multifractal models indicate that high grade mineralization is  
27 situated in the central and southern parts of the ore deposit. Their results are compared  
28 with the alteration and mineralogical models resulted from the 3D geological model

29 using logratio matrix. The results show that the S-V model gives the best results to  
30 identify highly mineralized zones in the deposit. However, the results of C-V model for  
31 moderately and weakly mineralized zones are more accurate than the zones obtained  
32 from the N-S and S-V model.

33 Keywords: Fractal; Concentration-volume model (C-V); Number-size model (N-S);  
34 Power spectrum-volume model (S-V); Mineralized zone; the Pulang porphyry copper  
35 deposit

## 36 **1. Introduction**

37 The definition and delineation of different mineralized zones and non-mineralized  
38 wall rocks are the main purpose in the economic geology and mineral exploration.  
39 Investigation of ore mineralogy and paragenetic sequence provides useful data on  
40 ore-forming processes in deposits, because the typical characteristics of various types  
41 of ore deposits are reflected by their mineral assemblages (Craig and Vaughan, 1994;  
42 White and Hedenquist, 1995). Common methods are usually based on mineralography,  
43 petrography and alteration minerals assemblages to delineate various mineralized  
44 zones in porphyry deposits (Beane, 1982; Schwartz, 1947; Sillitoe, 1997; Berger et al.,  
45 2008). Lowell (1968) firstly proposed a conceptual model of lateral and vertical  
46 variations in mineralogy within alteration zones. Some similar models were developed  
47 related to potassic alteration usually situated in the center and deep parts of porphyry  
48 ore deposits based on this model (Sillitoe and Gappe, 1984; Cox and Singer, 1986;  
49 Melfos et al., 2002). Fluid inclusion and stable isotope studies are other methods to  
50 outline different mineralization phases based on thermometric and isotope element  
51 parameters along with other geological particulars (e.g., Boyce et al., 2007; Faure et al.,  
52 2002; Wilson et al., 2007). The drillhole data with a logging information containing  
53 mineralogical information, host rock changes and alteration is helpful to delineate  
54 the mineralization zones. Different geological interpretations could be presented to  
55 detect zone boundaries, which may also lead to different results because the elemental  
56 grade distribution may not be taken into consideration.

57 Non-Euclidian fractal geometry (Mandelbrot, 1983) is an important branch of

58 non-linear mathematical sciences, which is applied in various research fields of  
59 geosciences since the 1980s. The relationships between geology, geochemistry and  
60 mineralogical settings with spatial information can be researched by the methods  
61 based on fractal geometry (Afzal et al., 2011; Carranza, 2008, 2009). Bolviken et al.  
62 (1992) and Cheng et al. (1994) have shown that geochemical patterns of various  
63 elements have fractal dimensions. The concentration-area (C-A) model was proposed  
64 by Cheng et al. (1994) to recognize geochemical anomalies from backgrounds and  
65 calculate elemental thresholds of different geochemical data. Furthermore, there are  
66 many other fractal models proposed and applied in geochemical exploration work  
67 including number-size (N-S) fractal model proposed by Mandelbrot (1983) and  
68 Agterberg (1995), power spectrum-area (S-A) fractal model proposed by Cheng et  
69 al.(1999), concentration-distance (C-D) fractal model proposed by Li et al. (2003),  
70 concentration-volume (C-V) fractal model proposed by Afzal et al. (2011) and power  
71 spectrum-volume (S-V) fractal model proposed by Afzal et al. (2012).

72 Methods of fractal analysis also serve to illustrate relationships of geological,  
73 geochemical and mineralogical settings with spatial information derived from analysis  
74 of mineral deposit occurrence data (Carranza, 2008; Carranza et al., 2009; Goncalves  
75 et al., 2001). Various geochemical processes can be described based on differences in  
76 fractal dimensions obtained from analysis of relevant geochemical data. Afzal et al.  
77 (2011) considered that the log-log plots obtained by fractal methods are useful tools to  
78 delineate different geological populations of geochemical data and the thresholds could  
79 be determined as some break points in those plots.

80 The application of fractal models to delineate various grade mineralization zones  
81 was dependent on the relationships between metal grades and volumes (Afzal et al.,  
82 2011; Agterberg et al., 1993; Cheng, 2007; Simet et al., 1999; Turcotte, 1986). Afzal et al.  
83 (2011 and 2012) proposed concentration-volume (C-V) and power spectrum-volume  
84 (S-V) fractal model to delineate different porphyry-Cu mineralized zones and barren  
85 host rocks. In this paper, N-S, C-V and S-V fractal models were applied to delineate  
86 various mineralized zones and barren host rocks in the Pulang porphyry copper deposit,  
87 Yunnan, SW China.

## 88 2. Fractal models

### 89 2.1. Number-size (N-S) fractal model

90 Number-size (N-S) method proposed by Mandelbrot (1983) can be utilized to  
91 describe the distribution of geochemical populations (Sadeghi et al., 2012). In this  
92 method, geochemical data do not undergo any pre-processing (Mao et al., 2004). This  
93 model shows a relationship between desirable attributes (e.g. Cu concentration in this  
94 study) and their cumulative number of samples (Sadeghi et al., 2012). A power-law  
95 frequency model has been proposed to explain the N-S relationship according to the  
96 frequency distribution of elemental concentrations and cumulative number of samples  
97 with those attributes (e.g., Li et al., 1994; Sadeghi et al., 2012; Sanderson et al., 1994;  
98 Shi and Wang, 1998; Turcotte, 1996; Zuo et al., 2009a).

99 The N-S model proposed by Mandelbrot (1983) has been expressed as follows:

$$100 \quad N(\geq\rho)=F\rho^{-D} \quad (1)$$

101 where  $\rho$  denotes element concentration,  $N(\geq\rho)$  denotes cumulative number of samples  
102 with concentration values greater than or equal to  $\rho$ ,  $F$  is a constant and  $D$  is the scaling  
103 exponent or fractal dimension of the distribution of element concentrations. According  
104 to Mandelbrot (1983), log-log plots of  $N(\geq\rho)$  versus  $\rho$  show straight line segments  
105 with different slopes  $-D$  corresponding to different concentration intervals.

### 106 2.2. Concentration-volume (C-V) fractal model

107 Afzal et al.(2011) proposed concentration-volume (C-V) fractal model based on  
108 the same idea as the concentration-area (C-A) model (Cheng et al., 1994) to analysis  
109 the relationship between the concentration of ore elements and accumulative volume  
110 with concentration greater than or equal to the given value (Afzal et al., 2011; Zuo et  
111 al., 2016; Lin et al., 2013; Sadeghi et al., 2012; Soltani et al., 2014; Sun and Liu, 2014;  
112 Wang, G. et al., 2012). It can be expressed as:

$$113 \quad V(\rho\leq v)\propto\rho^{-a_1}; V(\rho\geq v)\propto\rho^{-a_2} \quad (2)$$

114  $V(\rho\geq v)$  and  $V(\rho\leq v)$  represent those occupied volumes with concentrations above or  
115 equal to and less than or equal to the contour value  $v$ ;  $v$  indicates the threshold value of

116 a zone;  $a_1$  and  $a_2$  are the characteristic indexes. Thresholds obtained by this method  
117 indicate the boundaries between different grade mineralization zones and barren host  
118 rocks of ore deposits. The drillhole data of elemental concentration values were  
119 interpolated by using geostatistical estimation to compute  $V(\rho \geq v)$  and  $V(\rho \leq v)$ , which  
120 are the volume values enclosed by a contour level  $\rho$  in a 3D model.

### 121 2.3. Power spectrum-volume (S-V) fractal model

122 Different geochemical patterns in the spatial domain could be seen as layered  
123 signals of various frequencies. Cheng et al. (1999) proposed the power spectrum-area  
124 (S-A) fractal model to recognize geochemical anomalies from backgrounds utilizing  
125 the method of spectrum analysis in frequency domain according to this argument. This  
126 model is combined with concentration-area (C-A) model (Cheng et al. 1994). It offers  
127 an useful tool to determine an optimum threshold value between various patterns based  
128 on the scaling property.

129 Afzal et al.(2012) proposed the power spectrum-volume (S-V) fractal model to  
130 delineate different grade mineralization zones based on the same idea as the S-A model  
131 proposed by Cheng et al.(1999). S-V model was utilized in frequency domain. And it  
132 was performed by applying the fast Fourier transformation for assay data. The straight  
133 lines obtained by log-log plots indicate the relationships between power spectrums and  
134 relevant volumes of ore elements. They were utilized to recognize the hypogene zones  
135 and supergene enrichment zones from barren host rocks and leached zone of the  
136 deposit. The recognition of various mineralization zones is on the basis of the  
137 power-law relationships between power spectrums and occupied volumes. The formula  
138 is as follows:

$$139 \quad V(\geq S) \propto S^{-2/\beta} \quad (3)$$

140 Where, the power-law relationships between power spectrums ( $S = -\|F(W_x, W_y,$   
141  $W_z)\|$ ) and occupied volumes with power spectrums greater than or equal to  $S$  can be  
142 indicated by this form;  $F$  represents the fast Fourier transformation of the measurement  
143  $\mu(x, y, z)$ ;  $W_x, W_y$  and  $W_z$  respectively indicate wave numbers or angular frequencies  
144 in X, Y and Z axes directions on a 3D model. The range of index  $\beta$  is  $0 < \beta \leq 2$  or  $1 \leq 2/\beta$

145 with the special case of  $\beta=2$  or  $2/\beta=1$  corresponding to non-fractal or monofractal and  
146  $1<2/\beta$  to multifractals (Cheng, 2006).

147 By using the method of geostatistical estimation, the drillhole data of elemental  
148 concentration values were interpolated to construct the block model with ore element  
149 distribution. The power spectrum values can be obtained by using 3D fast Fourier  
150 transformation for ore element grades. The logarithm of all power spectrum values and  
151 accumulative volume values were calculated. And the log-log plot between power  
152 spectrums and volumes was drawn according to previous counted values. Then the  
153 filters were constructed on the basis of threshold values obtained by the log-log plot of  
154 S-V. Finally, the power spectrums were converted back to the space domain by  
155 utilizing inverse fast Fourier transformation.

### 156 **3. Geological setting of the Pulang porphyry copper deposit**

157 The Pulang porphyry copper deposit is situated in the southern end of the Yidun  
158 continental arc, southwest China (Fig.1). The continental arc was produced due to the  
159 westward subduction of Garze–Litang oceanic crust (Deng et al., 2014b, 2015; Wang et  
160 al., 2014). And the Pulang ore deposit, one of the largest porphyry copper deposits in  
161 China (Deng et al., 2012, 2014a; Mao et al., 2012, 2014), is characterized by typical  
162 porphyry-type alteration zone. The geological characteristics of the deposit, including  
163 the alteration types and their zonation, the geometry of orebody, metallogenic time and  
164 the geodynamic settings have been systematically researched (Leng et al., 2012; Li et al.,  
165 2011, 2013). The deposit consists of five ore-bearing porphyry bodies, covering an area  
166 of approximately 9 km<sup>2</sup>, and the explored ore tonnage of Cu is estimated to be 6.50 Mt  
167 (Liu et al., 2013).

168 The outcrop strata of Pulang deposit are dominated by Upper Triassic Tumugou  
169 Formation clastic rocks and andesite, and Quaternary sediments (Fig.1c). The Triassic  
170 porphyry intrusions primarily comprise quartz diorite porphyry, quartz monzonite  
171 porphyry, quartz diorite porphyrite and granodiorite porphyry. The Tumugou Formation  
172 strata was intruded by the quartz diorite porphyry with an age of  $219.6 \pm 3.5$  Ma  
173 (Zircon U-Pb dating) (Pang et al., 2009). Then quartz monzonite porphyry with an age

174 of  $212.8 \pm 1.9$  Ma and granodiorite porphyry with an age of  $206.3 \pm 0.7$  Ma (Zircon  
175 U-Pb dating) (Liu et al., 2013) crosscut quartz diorite porphyry, respectively. The  
176 quartz monzonite porphyry is considered to be associated with mineralization because  
177 its age is similar with the molybdenite Re-Os isochron age of  $213 \pm 3.8$  Ma from  
178 orebody (Zeng et al., 2004). Moreover, the Cu concentrations of quartz monzonite  
179 porphyry are higher than the other porphyries.

180 The porphyry-type alteration zones transit upward and outward from early  
181 potassium-silicate, through quartz-sericite to propylitization from the core of the quartz  
182 monzonite porphyry (Fig. 4). The wall rocks near the porphyries were mostly changed  
183 into hornfels. Systematic drilling has demonstrated that the potassium-silicate and  
184 quartz-sericite zones host the main orebodies, constituting the core of mineralized  
185 zones. And the propylitic zones and hornfels only develop the weak mineralization.  
186 The orebodies occur mainly in potassium-silicate and quartz-sericite, and occur as  
187 veins in the propylitic zones and hornfels. Major rock types in the deposit are quartz  
188 monzonite porphyry, quartz diorite porphyrite, granite diorite porphyry, quartz diorite  
189 porphyry and hornfels (Fig.2). Metallic minerals mainly include pyrite, chalcopyrite  
190 with small amount of molybdenite and pyrrhotite (Fig. 3).

#### 191 **4. Fractal modeling**

192 Based on the geological data (which include collar coordinates of each drillhole,  
193 azimuth and dip (orientation), lithology and mineralogy) recorded from 130 drillholes  
194 in Pulang deposit, 20492 lithogeochemical samples have been collected at 2 m  
195 intervals. The laboratory of the 3rd Geological Team of the Yunnan Bureau of Geology  
196 and Mineral Resources utilized the iodine-fluorine and oscillo-polarographic method to  
197 analyze the concentrations of Cu and associated paragenetic elements and its analytical  
198 uncertainty is less than 7% (Yunnan Diqing Nonferrous Metal Co. Ltd., 2009). Only  
199 Cu concentrations were researched in this study. The distribution of Cu concentrations  
200 is log-normal (Fig. 5). The experimental semi-variogram of Cu data of Pulang deposit  
201 indicates a range and nugget effect of 320.0m and 0.25, separately (Fig. 6). The  
202 spherical model is fitted in regard to the experimental semi-variogram. The 3D model

203 of Cu concentrations distribution of Pulang deposit was produced with ordinary kriging  
204 method using the Geovia Surpac software on the basis of the semi-variogram and  
205 anisotropic ellipsoid. Fundamentally, the accuracy of the interpolation results mainly  
206 depends on whether the interpolation model could well fit the spatial distribution  
207 characteristics of the deposit. Ordinary kriging was used because it is compatible with  
208 a stationary model; it only involves a variogram, and it is in fact the form of kriging  
209 used most (Chilès and Delfiner, 1999). Goovaerts (1997) showed that the values in  
210 un-sampled locations are estimated by the ordinary kriging method according to  
211 moving average of the interest variables satisfying various distribution forms of data. It  
212 is a spatial estimation method where the error variance is minimized. This error  
213 variance is based on the configuration of the data and its variogram (Yamamoto, 2005).  
214 The correct variogram in kriging interpolation can guarantee the accuracy of the  
215 interpolation results.

216 The accuracy of the spatial interpolation analysis is verified by comparing the  
217 difference between the measured values and the predicted values, so as to select the  
218 best variogram model. In order to test the variogram model, the cross-validation  
219 method was used to determine whether the parameters of the variogram model are  
220 correct. The distribution of the residual is normal (Fig.7) and the mean of error between  
221 the actual and estimated Cu grade values is equal to 0 (Table 1). It indicates that this  
222 model is reasonable, and the variogram parameters are unbiased for estimating the Cu  
223 grade.

224 The obtained block models were used as input to the fractal models. The Pulang  
225 deposit was modeled by 20m×20m×5m voxels and they were decided by the grid  
226 drilling dimensions and geometrical properties of the deposit (David, 1970). The  
227 Pulang deposit is totally modeled with 150,973 voxels. The terms of “highly”,  
228 “moderately” and “weakly” have been used to classify the mineralized zones based on  
229 fractal modeling and accordance with the classification of in terms of ore grades in the  
230 deposit.

#### 231 **4.1 Number-size (N-S) fractal modeling**



232 The N-S model was applied to the Cu data (Fig. 8). The selection of breakpoints as  
233 threshold values appears to be an objective decision because geochemical populations  
234 are defined by different line segments in the N-S log-log plot. The straight fitted lines  
235 were obtained based on least-square regression (Agterberg et al., 1996; Spalla et  
236 al.,2010). In other words, the intensity of element enrichment is depicted by each slope  
237 of the line segment in the N-S log-log plots (Afzal et al., 2010; Bai et al., 2010).

238 Based on the classification of the 3D model of Cu data and the thresholds obtained  
239 from N-S fractal model (Table 2), highly mineralized zones are situated in the southern  
240 and central parts of Pulang deposit that coincide with the potassium-silicate alterations.  
241 However, small highly mineralized zones are located in the central parts of the Pulang  
242 deposit (Fig.9). Moderately mineralized zones are disposed in a northwest-southeast  
243 trend correlated with phyllic zones. Weakly mineralized zones and barren host rocks  
244 are situated in the marginal parts of the area.

#### 245 **4.2. Concentration-volume (C-V) fractal modeling**

246 The occupied volume values corresponding to Cu grades were computed to obtain  
247 the concentration-volume model according to the 3D model of Pulang deposit.  
248 Through the obtained C-V log-log plot, the threshold values of Cu grades were  
249 determined (Fig.10). It indicates the power-law relationships between Cu grades and  
250 volumes. According to these results (Table 3), the low concentration zones exist in  
251 many parts of the deposit and are disposed along the NW-SE trend. Moderately and  
252 highly mineralized zones are situated in several parts of the center and south of the  
253 deposit (Fig. 11).

#### 254 **4.3. Power spectrum-volume (S-V) fractal modeling**

255 Based on the geological data (which include collar coordinates of each drillhole,  
256 azimuth and dip (orientation), lithology and mineralogy) recorded from 130 drillholes  
257 in the deposit, a 3D model and block model of the distribution of Cu in Pulang deposit  
258 were constructed with ordinary kriging using the Geovia Surpac software.

259 The power spectrum (S) were calculated for the 3D elemental distribution using  
260 3D fast Fourier transformation by MATLAB (R2016a). The logarithmic values of

261 power spectrums and relevant volume values were plotted against each other (Fig. 12).  
262 The straight lines fitted through log-log plot indicate different relationships between  
263 power spectrums and occupied volumes. The thresholds of  $\log S=7.81$  and  $\log S=8.70$   
264 were decided by the log-log S-V plot. The 3D filters were designed to separate  
265 different mineralization zones on the basis of these threshold values. Inverse fast  
266 Fourier transformation was used to convert the decomposed components back into the  
267 space domain by MATLAB (R2016a). According to the results, Cu concentrations of  
268 the hypogene zones range from 0.23% to 1.33% (Table 4), and values of  $>1.33\%$  Cu  
269 refer to the supergene enrichment zones, whereas values of  $<0.23\%$  Cu pertain to the  
270 leached zone and barren host rocks (Fig. 13).

## 271 **5. Comparison of fractal models and geological model of the deposit**

272 Alteration models have a key role in zone delineation and also in presenting  
273 geological models, as described by Lowell and Guilbert (1970). The potassic and  
274 phyllic alterations control major mineralization within supergene enrichment and  
275 hypogene zones according to these models. Models of Cu mineralization zones derived  
276 via the fractal models can be compared with geological data in order to validate the  
277 results of analysis in different porphyry Cu deposits. Results of fractal modeling of  
278 Pulang deposit were compared with the 3D geological model of the deposit constructed  
279 by using the Geovia Surpac software and drillhole data (Fig. 2). Moreover, the results  
280 obtained from these fractal models are controlled by mineralogical investigations.

281 Carranza (2011) has illustrated an analysis for calculation of spatial correlations  
282 between two binary especially mathematical and geological models. An intersection  
283 operation between the mineralization zones obtained from fractal models and different  
284 alteration zones in the geological model was performed to derive the amount of voxels  
285 corresponding to each of the classes of overlap zones (Table 5). Using the obtained  
286 numbers of voxels, Type I error (T1E), Type II error (T2E), and overall accuracy (OA)  
287 of the fractal model were estimated with respect to different alteration zones due to  
288 geological data (Carranza, 2011). The values of OA of fractal models of mineralized  
289 zones were compared with each other as follows.

290 A comparison between highly mineralized zones based on the fractal models and  
291 potassic alteration zones resulted from the 3D geological model shows that there is a  
292 similarity among these fractal models. Overall accuracies for the C-V, N-S and S-V  
293 models are 0.50, 0.51 and 0.52, respectively (Table 6), which indicate that the S-V  
294 model gives better results to identify highly mineralized zones in the deposit. Because  
295 the fact that the number of overlapped voxels (A) in the S-V model is higher than those  
296 in N-S and C-V model. The correlation (from OA results) between highly mineralized  
297 zones obtained from S-V modeling and the potassic alteration zones is better than the  
298 N-S and C-V model because of a strong proportional relationship between extension  
299 and positions of voxels in the S-V model and potassic alteration zones in the 3D  
300 geological model.

301 Comparison between phyllic alteration zones resulted from the 3D geological  
302 model and moderately and weakly mineralized zones from fractal modeling shows that  
303 overall accuracies of the C-V, N-S and S-V fractal models with respect to phyllic  
304 alteration zones of the geological model are 0.59, 0.56 and 0.54, respectively. Overall  
305 accuracy value of moderately and weakly mineralized zones obtained from C-V  
306 modeling is higher than the mineralized zones obtained from N-S and S-V modeling  
307 (Table 7). On the other hand, moderately mineralized zones defined by C-V modeling  
308 have overlap with the phyllic zones in the 3D geological model. However, the results  
309 of the C-V model are more accurate than those of the N-S and S-V model with respect  
310 to the phyllic zones in the 3D geological model.

311 It could be considered that there are spatial correlations between different  
312 modeled Cu zones and geological features such as alterations and mineralogy. Several  
313 samples were collected from different drillholes in different grade mineralization zones  
314 of Pulang deposit to validate the results of fractal models. They were analyzed by  
315 microscopic identification and XRF (X-ray Fluorescence Spectrometer). The PL-B82  
316 sample was collected from the drillhole situated in the high grade mineralization zones.  
317 There are high chalcopyrite content and some molybdenite (Fig.16a). PL-B62 sample  
318 was collected from the drillhole situated in the moderate grade mineralization zones.  
319 There are low chalcopyrite content and some pyrrhotite content in polished section

320 (Fig.16b). PL-B74 sample was collected from the drillhole located at the weakly  
321 mineralized zones with lower chalcopyrite content and some pyrrhotite (Fig.16c and  
322 Fig.16d). Results obtained from mineralogy, microscopic identification and drillhole  
323 scanning by XRF of these samples indicates that Cu concentrations are 1.80%, 1.32%  
324 and 0.41% in PL-B82, PL-B62 and PL-B74 samples, respectively (Table 8).

## 325 **6. Conclusions**

326 In the many cases, drillhole logging is dealing with the lack of proper diagnosis of  
327 geological phenomenon and it can undermine delineation of mineralized zones because  
328 it depends on the interpretation of individual loggers, which is subjective and no two  
329 loggers have the same interpretations. However, the conventional geological modeling  
330 based on drillhole data is fundamentally important for ore body spatial structure  
331 understanding and mathematical applications. Grades of the ore elements are not  
332 observed in conventional methods of geological ore modeling while the variations in  
333 ore grades in a mineral deposit is an obvious and salient feature. Given the problems as  
334 mentioned above, using a series of new established methods based on mathematical  
335 analyses such as fractal modeling seems to be inevitable.

336 In this paper, the number-size (N-S), concentration-volume (C-V) and power  
337 spectrum-volume (S-V) fractal models were used to delineate and recognize various  
338 Cu mineralized zones of Pulang porphyry copper deposit in the south end of the Yidun  
339 continental arc, SW China. All the fractal models reveal high grade Cu mineralized  
340 zones are situated in the central and southern parts of the deposit. The Cu threshold  
341 values of highly mineralized zones are 1.45% and 1.88% based on the N-S and C-V  
342 fractal models. And the Cu threshold of supergene enrichment zones is 1.33% based on  
343 the S-V fractal model. Models of moderately mineralized zones contain 0.28-1.45% Cu  
344 according to the N-S model, and 1.48-1.88% Cu according to the C-V model. The  
345 hypogene zones contain 0.23-1.33% Cu according to the S-V model. The N-S model  
346 reveals weakly mineralized zones and barren host rocks containing <0.28% Cu. In  
347 contrast, the C-V model reveals that barren host rocks contain <0.25% and weakly  
348 mineralized zones contain 0.25-1.48% Cu. And the S-V model reveals that barren host

349 rock and leached zone contain <0.23% Cu.

350 The comparison between highly mineralized zones based on the fractal models  
351 and potassic zones resulted from 3D geological model illustrates that the S-V fractal  
352 model is better than the N-S and C-V model because the fact that the number of  
353 overlapped voxels (A) in the S-V model is higher than those in the N-S and C-V  
354 model. Overall accuracies for the C-V, N-S and S-V models are 0.50, 0.51 and 0.52,  
355 respectively (Table 6), which indicate that the S-V model gives the best results to  
356 identify highly mineralized zones in the deposit. On the other hand, the correlation  
357 (from OA results) between highly mineralized zones obtained from S-V modeling and  
358 the potassic alteration zones is better than the N-S and C-V model because of a strong  
359 proportional relationship between extension and positions of voxels in the S-V model  
360 and potassic alteration zones in the 3D geological model.

361 Comparison between phyllic alteration zones resulted from the 3D geological  
362 model and moderate grade mineralization zones obtained from fractal models indicates  
363 that OA values of C-V, N-S and S-V fractal methods in regard to phyllic alteration  
364 zones of the geological model are 0.59, 0.56 and 0.54, respectively. Overall accuracy  
365 of moderately and weakly mineralized zones obtained from C-V modeling is higher  
366 than the mineralized zones obtained from N-S and S-V modeling (Table 7).

367 According to the correlation between the results driven by fractal modeling and  
368 geological logging from drillholes in the Pulang porphyry copper deposit, high grade  
369 mineralization zones generated by fractal models, especially the S-V model, has a  
370 better correlation with potassic alteration zones resulted from the 3D geological model  
371 than N-S and C-V model. The highly and moderately mineralized zones obtained from  
372 fractal models are both situated in the southern and central parts of the Pulang deposit  
373 that coincide with potassic and phyllic alteration zones. There is a better relationship  
374 between moderately and weakly mineralized zones derived by the C-V model and the  
375 phyllic alteration zones according to the 3D geological model than the N-S and S-V  
376 model.

377

378 **Acknowledgements**

379 This research was supported by the National Key R&D Program of China (201  
380 6YFC0600508). The authors thank Tao Dong, Haijun Yu, Qiwu Shen, Zhipeng  
381 Li, Baosheng Shi and Jinhong Yang for supporting in field investigation and pr-  
382 oviding parts of raw data.

383

384

385

386

387

388

389

390

391

392

393

394

395

396

397

398

399

400

401

402

403

404

405

406

407 **References**

- 408 Agterberg, F.P., Cheng, Q., and Wright, D.F.: Fractal modeling of mineral depos-  
409 -its, in: Proceedings of the 24th APCOM Symposium, Montreal, Canada, 43–53,  
410 1993.
- 411 Agterberg, F.P.: Multifractal modeling of the sizes and grades of giant and super  
412 giant deposits, *International Geology Review*, 37,1–8, [https://doi.org/10.1080/002](https://doi.org/10.1080/00206819509465388)  
413 [06819509465388](https://doi.org/10.1080/00206819509465388),1995.
- 414 Agterberg, F.P., Cheng, Q., Brown, A., Good, D.: Multifractal modeling of fractures in  
415 the Lac du Bonnet batholith, Manitoba. *Comput. Geosci.* 22, 497–507, 1996.
- 416 Afzal, P., Khakzad, A., Moarefvand, P., RashidnejadOmran, N., Esfandiari, B.,  
417 FadakarAlghalandis, Y.: Geochemical anomaly separation by multifractal modeling in  
418 Kahang (GorGor) porphyry system, Central Iran. *J. Geochem. Explor.* 104, 34–46,  
419 2010.
- 420 Afzal, P., Fadakar Alghalandis, Y., Khakzad, A., Moarefvand, P., and Rashidnejad  
421 Omran, N.: Delineation of mineralization zones in porphyry Cu deposits by fractal  
422 concentration–volume modeling, *J. Geochem. Explor.*, 108, 220–232, [https://doi.org/](https://doi.org/10.1016/j.gexplo.2011.03.005)  
423 [10.1016/j.gexplo.2011.03.005](https://doi.org/10.1016/j.gexplo.2011.03.005), 2011.
- 424 Afzal, P., Fadakar Alghalandis, A., Moarefvand, P., Rashidnejad Omran, N., and Asadi  
425 Haroni, H.: Application of power–spectrum–volume fractal method for detecting  
426 hypogene, supergene enrichment, leached and barren zones in Kahang Cu porphyry  
427 deposit, Central Iran, *J. Geochem. Explor.*, 112, 131–138, [https://doi.org/10.1016/](https://doi.org/10.1016/j.gexplo.2011.08.002)  
428 [j.gexplo.2011.08.002](https://doi.org/10.1016/j.gexplo.2011.08.002), 2012.
- 429 Bai, J., Porwal, A., Hart, C., Ford, A., Yu, L.: Mapping geochemical singularity using  
430 multifractal analysis: application to anomaly definition on stream sediments data from  
431 Funin Sheet, Yunnan, China, *J. Geochem. Explor.*, 104, 1–11, 2010.
- 432 Beane, R.E.: Hydrothermal alteration in silicate rocks, in: *Advances in Geology of the*  
433 *Porphyry Copper Deposits, Southwestern North America*, Titley, S.R. (Ed.),The  
434 University of Arizona Press, Tucson, 117–137, 1982.
- 435 Bolviken, B., Stokke, P.R., Feder, J., and Jossang, T.: The fractal nature of geo

436 chemical landscapes, *J. Geochem. Explor.*, 43,91–109, <https://doi.org/10.1016/0375>  
437 -6742(92)90001-O, 1992.

438 Boyce, A.J., Fulgnati, P., Sbrana, A., and Fallick, A.E.: Fluids in early stage hy-  
439 drothermal alteration of high-sulfidation epithermal systems: a view from the vol-  
440 cano active hydrothermal system (Aeolian Island, Italy), *Journal of Volcanology*  
441 and *Geothermal Research*, 166, 76–90, <https://doi.org/10.1016/j.jvolgeores.2007.07>.  
442 005, 2007.

443 Berger, B. R., Ayuso, R. A., Wynn, J. C., and Seal, R. R.: Preliminary Model of  
444 Porphyry Copper Deposits, USGS, Open-File Report, 1321 pp., 2008.

445 Cox, D. and Singer, D.: Mineral deposits models, *US Geological Survey Bulletin*, 1693  
446 pp., 1986.

447 Craig, G.R. and Vaughan, D.: *Ore Microscopy and Ore Petrography*, John Wiley  
448 and Sons, 1994.

449 Chilès, J.P. and Delfiner, P.: *Geostatistics: Modeling Spatial Uncertainty*, Wiley,  
450 New York, 695 pp., 1999.

451 Carranza, E.J.M.: Geochemical Anomaly and Mineral Prospectivity Mapping in GIS.  
452 *Handbook of Exploration and Environmental Geochemistry*, 11, Amsterdam, Elsevier,  
453 351 pp., 2008.

454 Carranza, E. J. M.: Controls on mineral deposit occurrence inferred from analysis of  
455 their spatial pattern and spatial association with geological features, *Ore Geol. Rev.*, 35,  
456 383–400, <https://doi.org/10.1016/j.oregeorev.2009.01.001>, 2009.

457 Carranza, E.J.M., Owusu, E.A., and Hale, M.: Mapping of prospectivity and estimation  
458 of number of undiscovered prospects for lode gold, southwestern Ashanti Belt, Ghana,  
459 *Mineralium Deposita*, 44, 915–938, <https://doi.org/10.1007/s00126-009-0250-6>, 2009.

460 Carranza, E.J.M.: From predictive mapping of mineral prospectivity to quantitative  
461 estimation of number of undiscovered prospects. *Resource Geology* 61, 30–51, 2010.

462 Carranza, E.J.M.: Analysis and mapping of geochemical anomalies using logratio  
463 -transformed stream sediment data with censored values, *J. Geochem. Explor.*, 1  
464 10, 167–185, <https://doi.org/10.1016/j.gexplo.2011.05.007>, 2011.

465 Cheng, Q., Agterberg, F.P., and Ballantyne, S.B.: The separation of geochemical



466 anomalies from background by fractal methods, *J. Geochem. Explor.*, 51, 109–130,  
467 [https://doi.org/10.1016/0375-6742\(94\)90013-2](https://doi.org/10.1016/0375-6742(94)90013-2), 1994.

468 Cheng, Q.: Spatial and scaling modelling for geochemical anomaly separation, *J.*  
469 *Geochem. Explor.*, 65, 175–194, [https://doi.org/10.1016/S0375-6742\(99\)00028-X](https://doi.org/10.1016/S0375-6742(99)00028-X),  
470 1999.

471 Cheng, Q.: Multifractal modelling and spectrum analysis: methods and applications to  
472 gamma ray spectrometer data from southwestern Nova Scotia, Canada, *Science in*  
473 *China, Series D: Earth Sciences* 49 (3), 283–294, 2006.

474 Cheng, Q.: Mapping singularities with stream sediment geochemical data for pre-  
475 -diction of undiscovered mineral deposits in Gejiu, Yunnan Province, China, *Ore*  
476 *Geol. Rev.*, 32, 314–324, <https://doi.org/10.1016/j.oregeorev.2006.10.002>, 2007.

477 David, M.: *Geostatistical Ore Reserve Estimation*, Amsterdam, Elsevier, 283 pp., 1970.

478 Deng, J., Wang, C.M., and Li, G.J.: Style and process of the superimposed minera-  
479 lization in the Sanjiang Tethys, *Acta Petrologica Sinica*, 28 (5), 1349–1361 (in  
480 Chinese with English abstract), 2012.

481 Deng, J., Wang, Q.F., Li, G.J., and Santosh, M.: Cenozoic tectono-magmatic and  
482 metallogenic processes in the Sanjiang region, southwestern China, *Earth Sci.*  
483 *Rev.*, 138, 268–299, <https://doi.org/10.1016/j.earscirev.2014.05.015>, 2014a.

484 Deng, J., Wang, Q.F., Li, G.J., Li, C.S., and Wang, C.M.: Tethys tectonic evolution and  
485 its bearing on the distribution of important mineral deposits in the Sanjiang region, SW  
486 China, *Gondwana Research*, 26 (2), 419–437, <https://doi.org/10.1016/j.gr.2013.08.002>,  
487 2014b.

488 Deng, J., Wang, Q.F., Li, G.J., Hou, Z.Q., Jiang, C.Z., and Danyushevsky, L.:  
489 Geology and genesis of the giant Beiya porphyry–skarn gold deposit, northwest-  
490 -ern Yangtze Block, China, *Ore Geol. Rev.*, 70, 457–485, <https://doi.org/10.1016/j.oregeorev.2015.02.015>, 2015.

492 Faure, K., Matsuhisa, Y., Metsugi, H., Mizota, C., and Hayashi, S.: The Hishika-  
493 ri Au–Ag epithermal deposit, Japan: oxygen and hydrogen isotope evidence in de-  
494 -termining the source of paleo hydrothermal fluids, *Economic Geology*, 97, 481  
495 –498, <https://doi.org/10.2113/gsecongeo.97.3.481>, 2002.

496 Goovaerts, P.: Geostatistics for Natural Resources Evaluation, Oxford University Press,  
497 New York, 496 pp. , 1997.

498 Goncalves, M. A., Mateus, A., and Oliveira, V.: Geochemical anomaly separation by  
499 multifractal modeling, *J. Geochem. Explor.*, 72, 91–114, [https://doi.org/10.1016/](https://doi.org/10.1016/S0375-6742(01)00156-X)  
500 [S0375-6742\(01\)00156-X](https://doi.org/10.1016/S0375-6742(01)00156-X), 2001.

501 Lowell, J.D.: Geology of the Kalamazoo orebody, San Manuel district, Arizona,  
502 *Economic Geology*, 63, 645–654, <https://doi.org/10.2113/gsecongeo.63.6.645>, 1968.

503 Lowell, J.D. and Guilbert, J.M.: Lateral and vertical alteration-mineralization zoning in  
504 porphyry ore deposits, *Economic Geology*, 65, 373–408, [https://doi.org/10.2113/](https://doi.org/10.2113/gsecongeo.65.4.373)  
505 [gsecongeo.65.4.373](https://doi.org/10.2113/gsecongeo.65.4.373), 1970.

506 Li, C., Xu, Y., Jiang, X.: The fractal model of mineral deposits. *Geol. Zhejiang* 10,  
507 25–32 (In Chinese with English Abstract), 1994.

508 Li, C., Ma, T., and Shi, J.: Application of a fractal method relating concentrations and  
509 distances for separation of geochemical anomalies from background, *J. Geochem.*  
510 *Explor.*,77, 167–175,[https://doi.org/10.1016/S0375-6742\(02\)00276-5](https://doi.org/10.1016/S0375-6742(02)00276-5), 2003.

511 Li, W.C., Zeng, P.S., Hou, Z.Q., and White, N.C.: The Pulang porphyry copper deposit  
512 and associated felsic intrusions in Yunnan Province, Southwest China, *Economic*  
513 *Geology*, 106 (1),79–92,<https://doi.org/10.2113/econgeo.106.1.79> , 2011.

514 Leng, C.B., Zhang, X.C., Hu, R.Z., Wang, S.X., Zhong, H., Wang, W.Q., and Bi, X.W.:  
515 ZirconU–Pb and molybdenite Re–Os geochronology and Sr–Nd–Pb–Hf isotopic  
516 constraintson the genesis of the Xuejiping porphyry copper deposit in Zhongdian,  
517 NorthwestYunnan, China, *Journal of Asian Earth Sciences* ,60, 31–48, 2012.

518 Liu, X.L., Li, W.C., Yin, G.H., and Zhang, N.: The geochronology, mineralogy and  
519 geochemistry study of the Pulang porphyry copper deposits in Geza arc of Yunnan  
520 Province, *Acta Petrologica Sinica*, 29(9), 3049–3064 (in Chinese with English abstract),  
521 2013.

522 Mandelbrot, B. B.: *The Fractal Geometry of Nature*, W. H. Freeman, San Fransisco,  
523 468 pp., 1983.

524 Melfos, V., Vavelidis, M., Christodes, G., and Seidel, E.: Origin and evolution of the  
525 Tertiary Maronia porphyry copper–molybdenum deposit, Thrace, Greece, *Mineralium*

526 Deposita, 37, 648–668, <https://doi.org/10.1007/s00126-002-0277-4>, 2002.

527 Mao, Z., Peng, S., Lai, J., Shao, Y., Yang, B.: Fractal study of geochemical prospecting  
528 data in south area of Fenghuanshan copper deposit, Tongling Anhui, *J. Earth Sci.*  
529 *Environ*, 26, 11–14, 2004.

530 Mao, J.W., Zhou, Z.H., Feng, C.Y., Wang, Y.T., Zhang, C.Q., Peng, H.J., and Yu, M.: A  
531 preliminary study of the Triassic large-scale mineralization in China and its  
532 geodynamic setting, *Geology in China*, 39(6), 1437–1471 (in Chinese with English  
533 abstract), 2012.

534 Mao, J.W., Pirajno, F., Lehmann, B., Luo, M.C., and Berzina, A.: Distribution of  
535 porphyry deposits in the Eurasian continent and their corresponding tectonic setti  
536 -ngs, *Journal of Asian Earth Sciences*, 79(PartB), 576–584, [https://doi.org/10.101](https://doi.org/10.1016/j.jseaes.2013.09.002)  
537 [6/ j.jseaes.2013.09.002](https://doi.org/10.1016/j.jseaes.2013.09.002), 2014.

538 Pang, Z.S., Du, Y.S., Wang, G.W., Guo, X., Cao, Y., and Li, Q.: Single-grain zircon  
539 U–Pb isotopic ages, geochemistry and its implication of Pulang complex in Yunnan  
540 Province, China, *Acta Petrologica Sinica*, 25(1), 159–165 (in Chinese with English  
541 abstract), 2009.

542 Pyrcz, M.J. and Deutsch, C.V.: *Geostatistical Reservoir Modeling*, Oxford University  
543 Press, 2014.

544 Sanderson, D.J., Roberts, S., Gumiel, P.: A fractal relationship between vein thickness  
545 and gold grade in drill core from La Codosera, Spain. *Econ. Geol.*, 89, 168–173, 1994.

546 Schwartz, G.M.: Hydrothermal alteration in the “porphyry copper” deposits, *Economic*  
547 *Geology*, 42, 319–352, <https://doi.org/10.2113/gsecongeo.42.4.319>, 1947.

548 Shi, J., Wang, C.: Fractal analysis of gold deposits in China: implication for giant  
549 deposit exploration. *Earth Sci. J. China Univ. Geosci.* 23, 616–618 (In Chinese with  
550 English abstract), 1998.

551 Sillitoe, R.H. and Gappe, I.M.: Philippine porphyry copper deposits: geologic setting  
552 and characteristics, *Common Coordination Joint Resource (CCOP)*, 14, 1–89, 1984.

553 Sillitoe, R.H.: Characteristics and controls of the largest porphyry copper–gold and  
554 epithermal gold deposits in the circum-pacific region, *Australian Journal of Earth*  
555 *Sciences*, 44, 373–388, <https://doi.org/10.1080/08120099708728318>, 1997.

556 Sim, B.L., Agterberg, F.P., and Beaudry, C.: Determining the cutoff between  
557 background and relative base metal contamination levels using multifractal methods,  
558 *Comput. Geosci.*, 25, 1023–1041, 1999.

559 Sadeghi, B., Moarefvand, P., Afzal, P., Yasrebi, A.B., and Saein, L.D.: Application of  
560 fractal models to outline mineralized zones in the Zaghia iron ore deposit, Central Iran,  
561 *J. Geochem. Explor.*, 122, 9–19, <https://doi.org/10.1016/j.gexplo.2012.04.011>, 2012.

562 Soltani, F., Afzal, P., and Asghari, O.: Delineation of alteration zones based on  
563 Sequential Gaussian Simulation and concentration–volume fractal modeling in the  
564 hypogene zone of Sungun copper deposit, NW Iran, *J. Geochem. Explor.*, 140, 64–76,  
565 <https://doi.org/10.1016/j.gexplo.2014.02.007>, 2014.

566 Spalla, M.I., Morotta, A.M., Gosso, G.: Advances in interpretation of geological  
567 processes: refinement of multi-scale data and integration in numerical modelling.  
568 Geological Society, London, 240 pp, 2010.

569 Sun, T. and Liu, L.: Delineating the complexity of Cu-Mo mineralization in a p-  
570 porphyry intrusion by computational and fractal modeling: A case study of the C-  
571 hehugou deposit in the Chifeng district, Inner Mongolia, China, *J. Geochem. Exp*  
572 *lor.*, 144, 128–143, <https://doi.org/10.1016/j.gexplo.2014.02.015>, 2014.

573 Turcotte, D.L.: A fractal approach to the relationship between ore grade and tonnage,  
574 *Economic Geology*, 18, 1525–1532, 1986.

575 Turcotte, D.L.: Fractals in geology and geophysics, *Pure Appl. Geophys.*, 131, 171–196,  
576 1989.

577 Turcotte, D.L.: *Fractals and Chaos in Geophysics*. second ed. Cambridge University  
578 Press, Cambridge UK, pp. 81–99, 1996.

579 White, N.C. and Hedenquist, J.W.: Epithermal gold deposits: styles, characteristics and  
580 exploration, *SEG Newsletter*, 23, 1–14, 1995.

581 Wilson, A.J., Cooke, David, R., Harper, B.J., and Deyell, C.L.: Sulfur isotopic zonation  
582 in the Cadia district, southeastern Australia: exploration significance and implications  
583 for the genesis of alkalic porphyry gold–copper deposits, *Mineralium Deposita*, 42,  
584 465–487, <https://doi.org/10.1007/s00126-006-0071-9>, 2007.

585 Wang, Q.F., Deng, J., Liu, H., Wang, Y., Sun, X., and Wan, L.: Fractal models f

586 -or estimating local reserves with different mineralization qualities and spatial v-  
587 ariations, *J. Geochem. Explor.*, 108, 196–208, [https://doi.org/10.1016/j.gexplo.2011.](https://doi.org/10.1016/j.gexplo.2011.02.008)  
588 02.008, 2011.

589 Wang, Q.F., Deng, J., Li, C.S., Li, G.J., Yu, L., and Qiao, L.: The boundary bet  
590 -ween the Simao and Yangtze blocks and their locations in Gondwana and Rodin  
591 -ia:constraints from detrital and inherited zircons, *Gondwana Research*, 26(2), 438  
592 –448,<https://doi.org/10.1016/j.gr.2013.10.002>, 2014.

593 Wang, G. W., Emmanuel John M. Carranza,Zuo, R., Hao, Y. L., Du, Y. S., Pang, Z. S.,  
594 and Sun Y.: Mapping of district-scale potential targets using fractal models, *J.*  
595 *Geochem. Explor.*, 122, 34–46, <https://doi.org/10.1016/j.gexplo.2012.06.013>, 2012.

596 Yamamoto, J.K.: Comparing Ordinary Kriging Interpolation Variance and Indicator  
597 Kriging Conditional Variance for Assessing Uncertainties at Unsampled Locations, in:  
598 *Application of Computers and Operations Research in the Mineral Industry*,edited by:  
599 Dessureault, S., Ganguli, R., Kecojevic, V., and Girard-Dwyer, J., Balkema, 2005.

600 Yunnan Diqing Nonferrous Metal Co. Ltd.:Exploration Report of Pulang Copper  
601 Deposit, Diqing, Yunnan, China, Yunnan Diqing Nonferrous Metal Co. Ltd., Diq  
602 ing Tibetan Autonomous Prefecture (in Chinese), 2009.

603 Zeng, P.S., Hou, Z.Q., Li, L.H., Qu, W.J., Wang, H.P., Li, W.C., Meng, Y.F., and Yang,  
604 Z.S.: Age of the Pulang porphyry copper deposit in NW Yunnan and its geological  
605 significance, *Geological Bulletin of China*, 23(11), 1127–1131 (in Chinese with  
606 English abstract), 2004.

607 Zuo, R., Cheng, Q., and Xia, Q.: Application of fractal models to characterization of  
608 vertical distribution of geochemical element concentration, *J. Geochem. Explor.*, 102,  
609 37–43,<https://doi.org/10.1016/j.gexplo.2008.11.020>, 2009.

610 Zuo, R. and Wang, J.: Fractal/multifractal modeling of geochemical data: A review, *J.*  
611 *Geochem. Explor.*, 164, 33-41, <https://doi.org/10.1016/j.gexplo.2015.04.010>, 2016.

612

613

614

615

616 **Fig.1.** Geological map of the Pulang porphyry copper deposit, SW China. Modified  
617 after Yunnan Diqing Nonferrous Metal Co. Ltd., 2009.

618 **Fig.2.** Geological 3D models including lithology, alteration and 3D drill hole plot with  
619 the legend of each in the Pulang porphyry copper deposit. (Scale is in  $m^3$ .)

620 **Fig.3.** Photographs of alteration and mineralization in the Pulang porphyry copper  
621 deposit, SW China.

622 (a) Quartz monzonite porphyry with potassium-silicate alteration; (b) Quartz diorite  
623 porphyrite with quartz-sericite alteration; (c) Quartz diorite porphyrite with propylitic  
624 alteration; (d) Hornfels. Qtz=quartz; Pl=plagioclase; Kfs=K-feldspar; Bt=biotite;  
625 Ser=sericite;Chl=chlorite; Ep=epidote; Py=pyrite; Ccp=chalcopyrite; Mo=molybdenite;  
626 Po= pyrrhotite.

627 **Fig.4.** Cross section along exploration line 0 in the Pulang porphyry copper deposit, SW  
628 China. Modified after Wang et al., 2012.

629 **Fig.5.** Histograms of the Cu raw (a) and logarithmic transformation (b) data in the  
630 Pulang deposit.

631 **Fig.6.** The experimental semi-variogram (omni-directional) of Cu data in Pulang  
632 deposit.

633 **Fig.7.** The cross-validation results: (a) residual VS Cu grade; (b) the residual di  
634 stribution histogram.

635 **Fig.8.** N-S log-log plot for Cu concentrations in the Pulang deposit.

636 **Fig.9.** Zones in the Pulang deposit based on thresholds defined from the N-S fractal  
637 model of Cu data: (a) highly mineralized zones; (b) moderately mineralized zones; (c)  
638 weakly mineralized zones and barren host rocks. (Scale is in  $m^3$ .)

639 **Fig.10.** C-V log-log plot for Cu concentrations in the Pulang deposit.

640 **Fig.11.** Zones in the Pulang deposit based on thresholds defined from the C-V fractal  
641 model of Cu data: (a) highly mineralized zones; (b) moderately mineralized zones; (c)  
642 weakly mineralized zones; (d) barren host rock.(Scale is in  $m^3$ .)

643 **Fig.12.** S-V log-log plot for Cu concentrations in the Pulang deposit.

644 **Fig.13.** Zones in the Pulang deposit based on thresholds defined from the S-V fractal  
645 model of Cu data: (a) the supergene enrichment zones; (b) the hypogene zones; (c) the  
646 leached zone and barren host rock (Scale is in  $m^3$ .)

647 **Fig.14.** Highly mineralized zones in the Pulang deposit: (a) potassium-silicate zone  
648 resulted from the 3D geological model from drillhole geological data; (b) N-S  
649 modeling of Cu data; and (c) C-V modeling of Cu data; (d) S-V modeling of Cu data  
650 (Scale is in  $m^3$ .)

651 **Fig.15.** Moderately mineralized zones in the Pulang deposit:(a) quartz-sericite zones  
652 resulted from the 3D geological model from drillhole geological data; (b) N-S  
653 modeling of Cu data; and (c) C-V modeling of Cu data; (d) S-V modeling of Cu data  
654 (Scale is in  $m^3$ .)

655 **Fig.16.** Chalcopyrite content in several samples based on mineralogical study: (a)  
656 PL-B82 sample was collected from the drillhole situated in the high grade  
657 mineralization zones.; (b) PL-B62 sample was collected from the drillhole situated in  
658 the moderately grade mineralization zones.; (c) and (d) PL-B74 sample was collected  
659 from the drillhole located at the weakly mineralized zones.

660 **Table 1** The results of statistical characteristics of the residual.  
661 **Table 2** Thresholds concentrations obtained by using N-S model based on Cu% in  
662 Pulang deposit.  
663 **Table 3** Thresholds concentrations obtained by using C-V model based on Cu% in  
664 Pulang deposit.  
665 **Table 4** Ranges of power spectrum (S) for different mineralization zones in Pulang  
666 deposit.  
667 **Table 5** Matrix for comparing performance of fractal modeling results with geological  
668 model. A, B, C, and D represent number of voxels in overlaps between classes in the  
669 binary geological model and the binary results of fractal models (Carranza, 2011).  
670 **Table 6** Overall accuracy (OA), Type I and Type II errors (T1E and T2E, respectively)  
671 with respect to potassic alteration zone resulted from geological model and threshold  
672 values of Cu obtained through C-V , N-S and S-V fractal modeling.  
673 **Table 7** Overall accuracy (OA), Type I and Type II errors (T1E and T2E, respectively)  
674 with respect to phyllic alteration zone resulted from geological model and threshold  
675 values of Cu obtained through C-V, N-S and S-V fractal modeling.  
676 **Table 8** Results of XRF analysis of samples collected from different mineralized zones  
677 in the Pulang porphyry copper deposit.

678

679

680

681

682

683

684

685

686

687

688

689

690

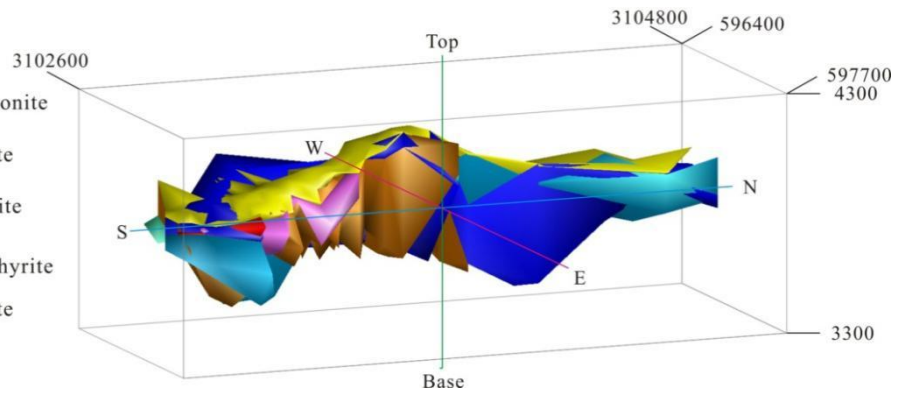
691





Lithology

- Qesl
- Quartz monzonite porphyry
- Quartz diorite porphyrite
- Granite diorite porphyry
- Diorite porphyrite
- Quartz diorite porphyry
- Hs

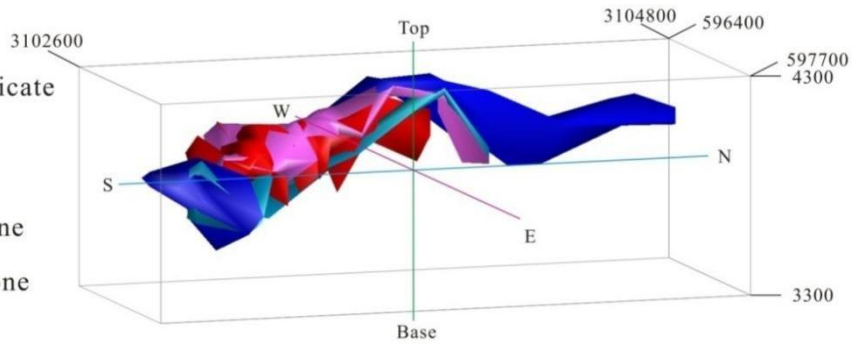


700

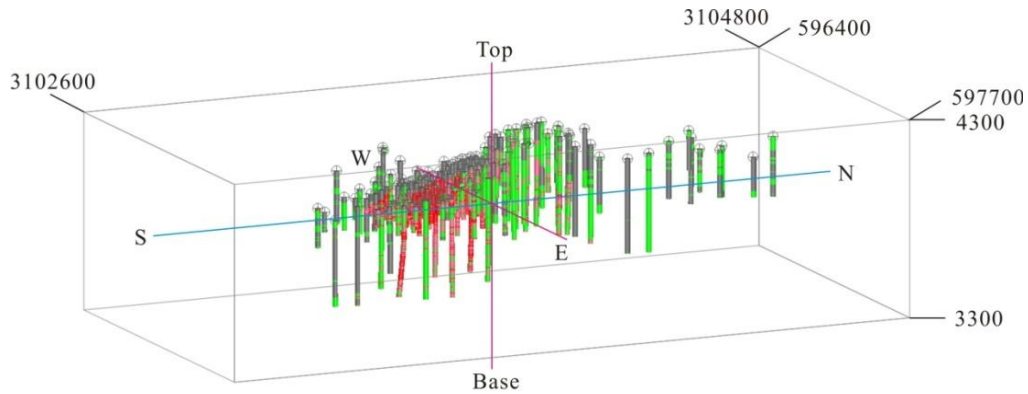
701

Alteration

- Potassium-silicate Zone
- Phyllic Zone
- Propylitic Zone
- Hornstone Zone



702



703

704

**Fig. 2.**

705

706

707

708

709

710

711

712

713  
714  
715  
716  
717  
718  
719  
720  
721  
722  
723  
724  
725  
726  
727  
728

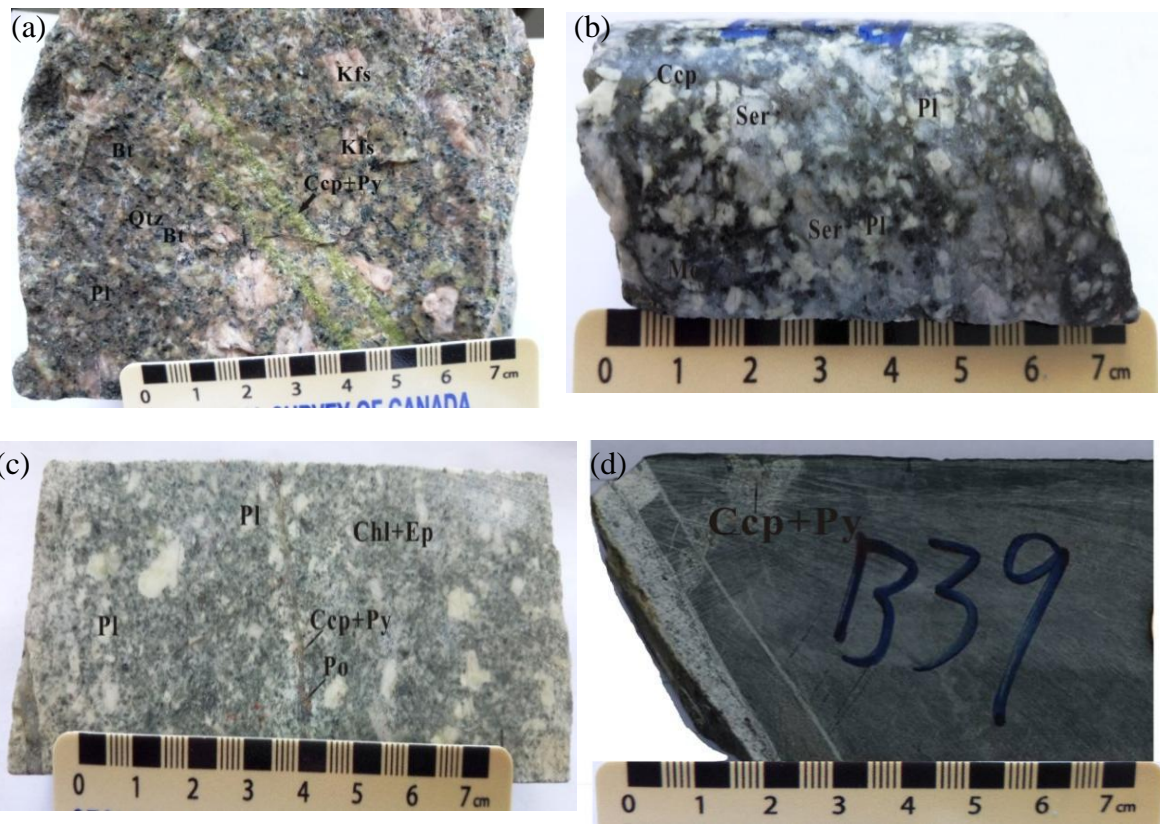


Fig. 3.

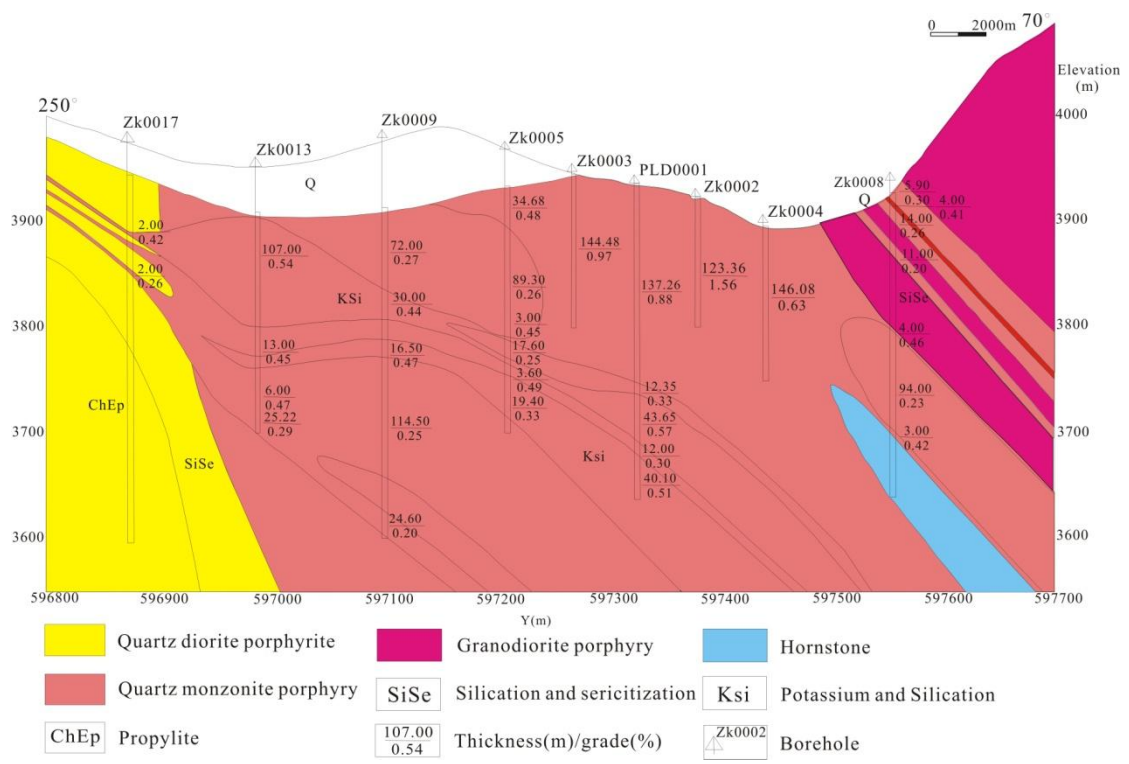
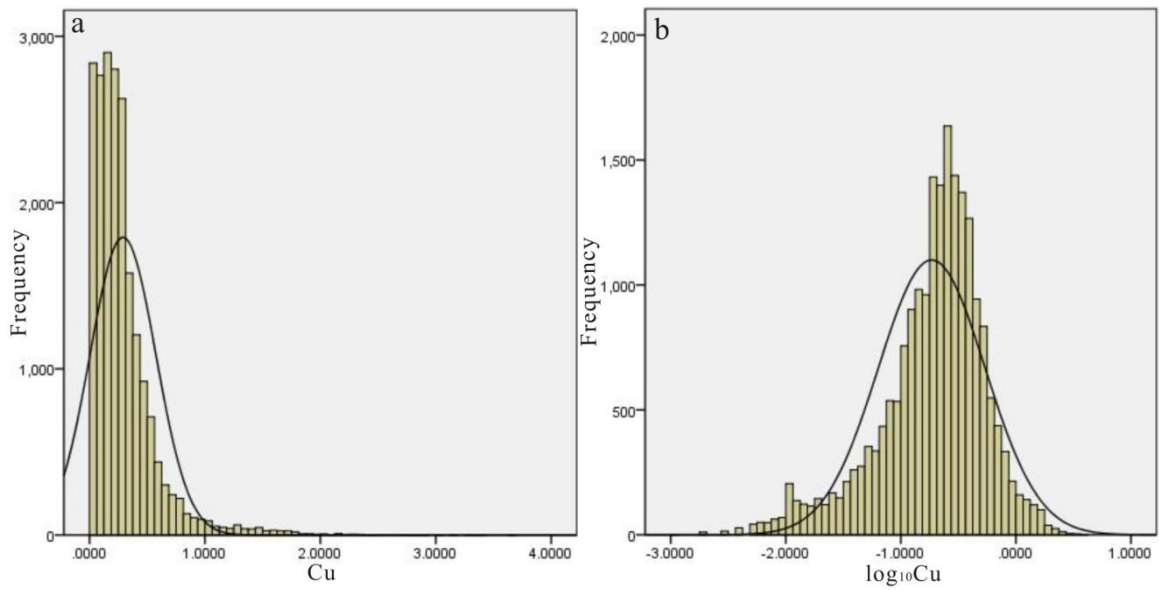


Fig. 4.

729  
730  
731

732  
733  
734  
735  
736  
737  
738  
739  
740  
741  
742



**Fig. 5.**

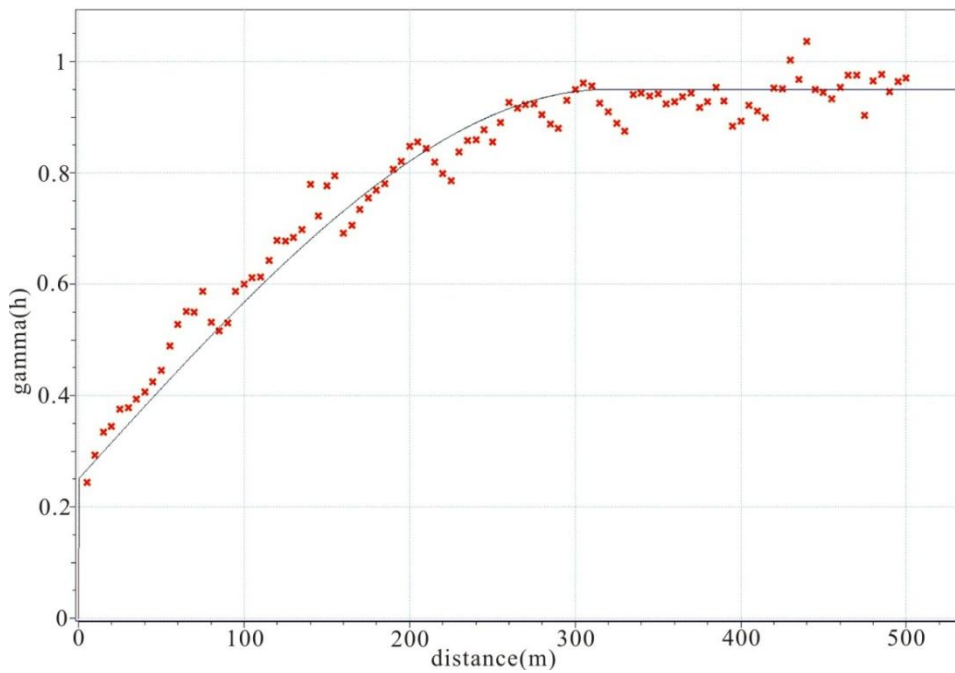


**Fig. 6.**

743  
744  
745  
746  
747  
748  
749  
750  
751

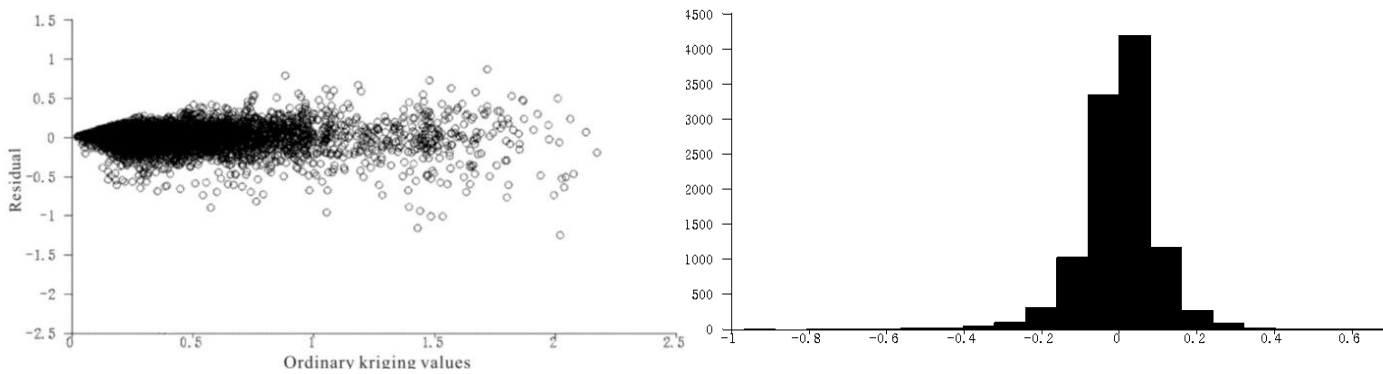
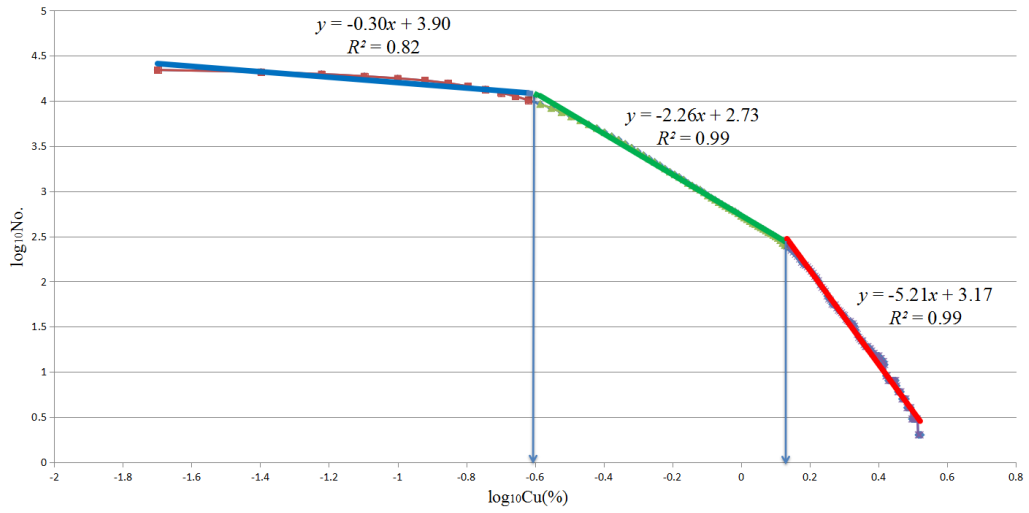


**Fig. 7.**

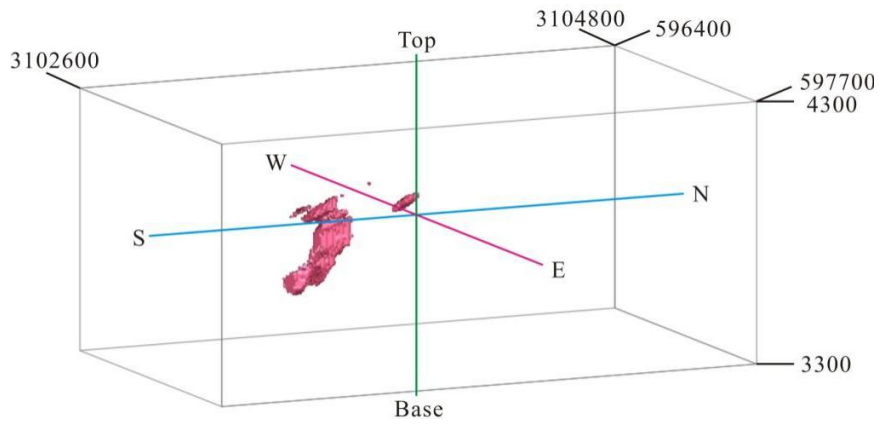


752

753

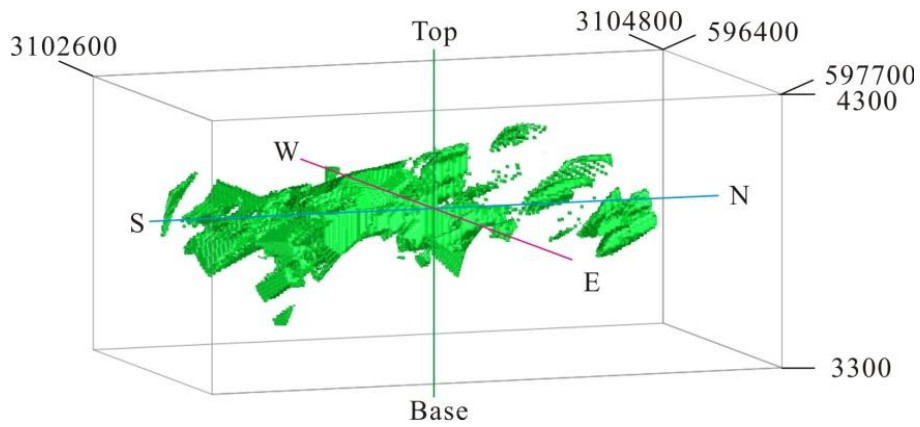
**Fig. 8.**

754 (a)



755

756 (b)



757

758

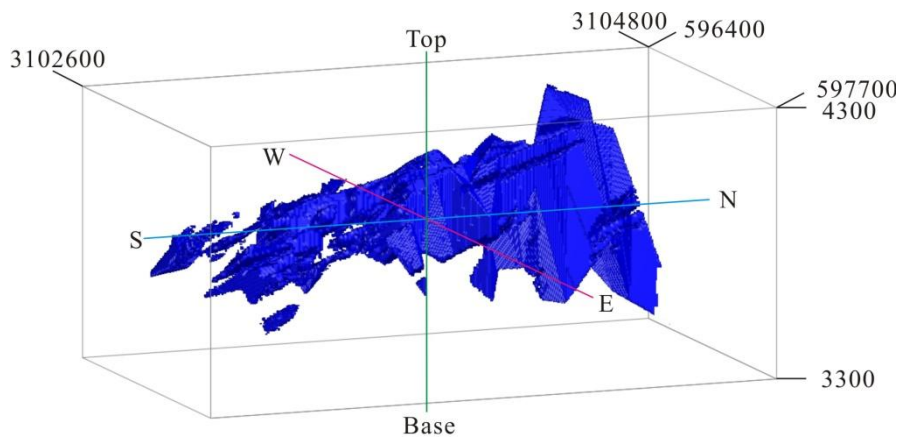
759

760

761

762

763 (c)



764

765

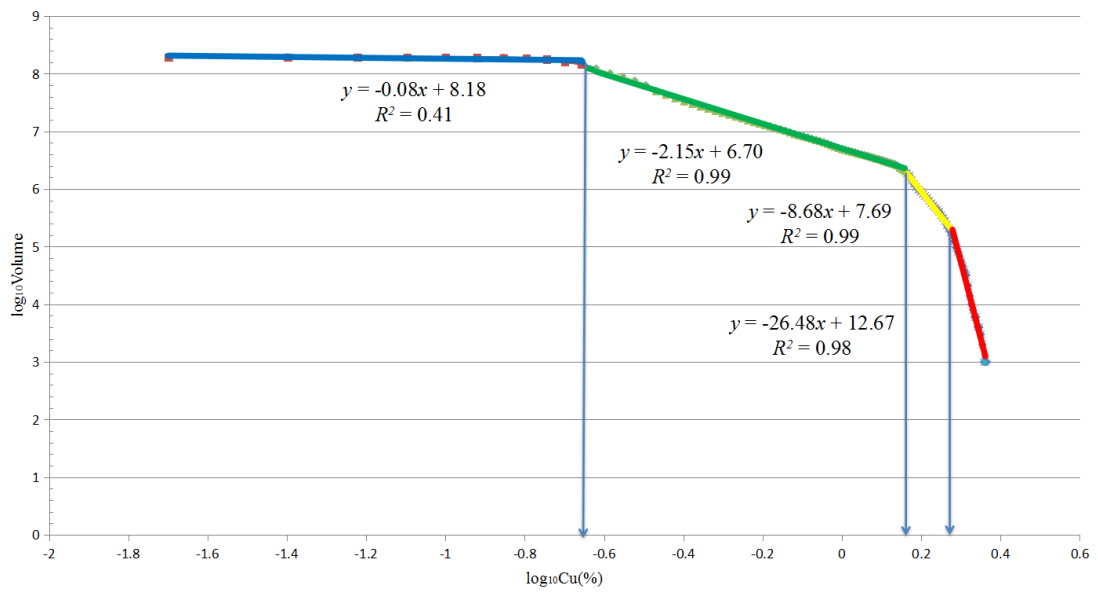
**Fig. 9**

766

767

768

769



770

771

**Fig. 10.**

772

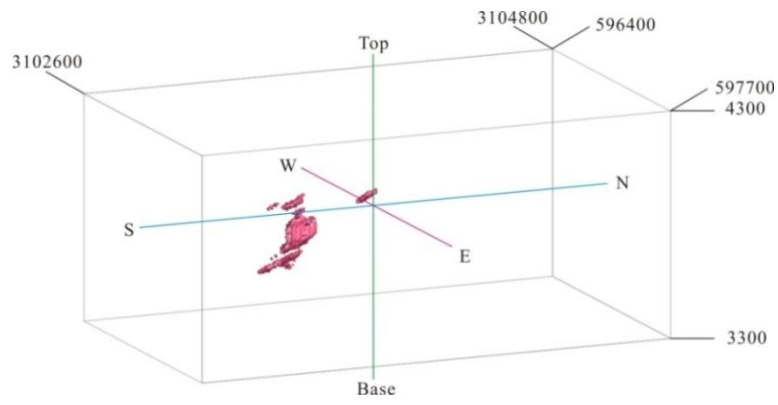
773

774

775

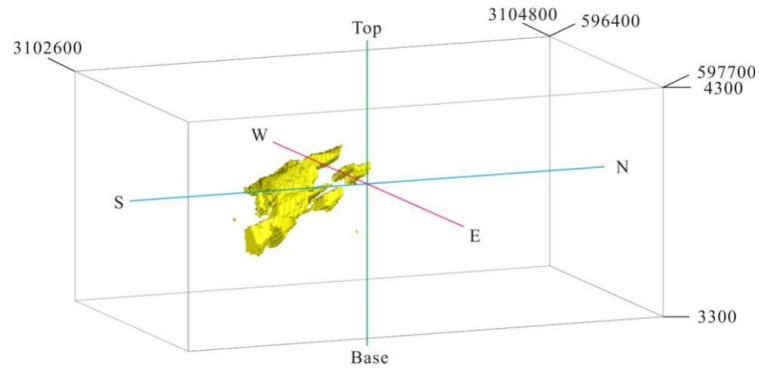
776

777 (a)



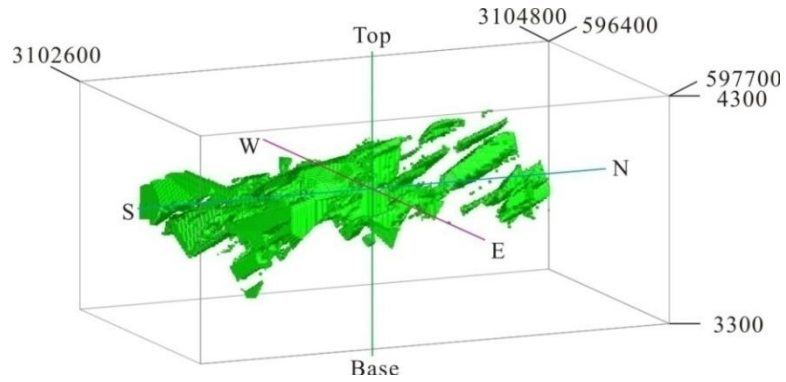
778

779 (b)



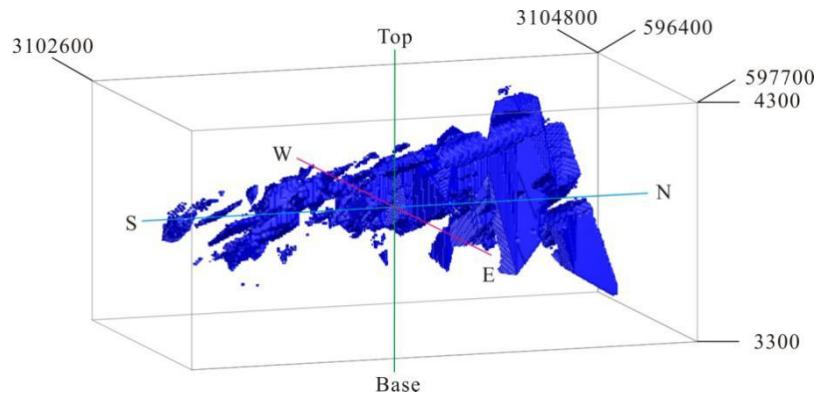
780

781 (c)



782

783 (d)



784

785

**Fig. 11.**

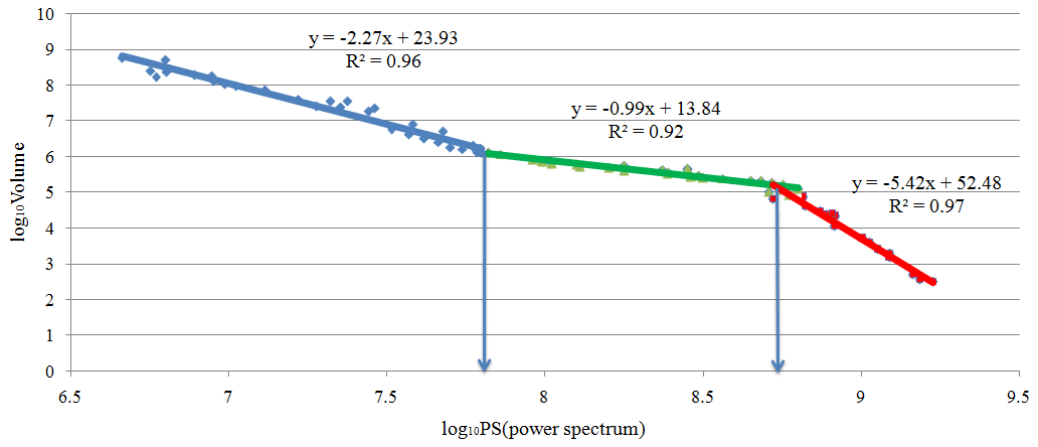
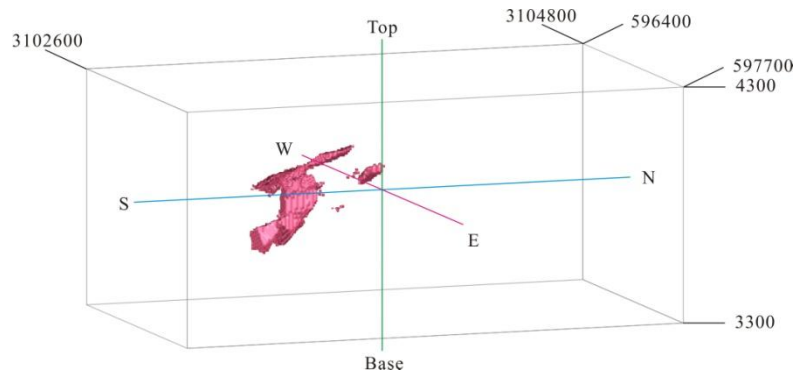


**Fig. 12.**

786

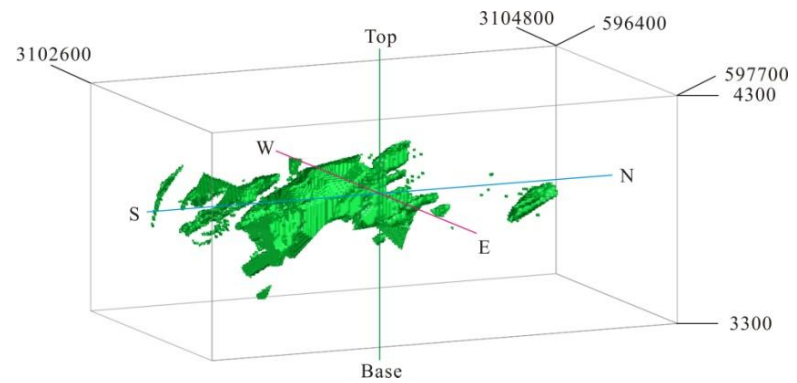
787

788 (a)



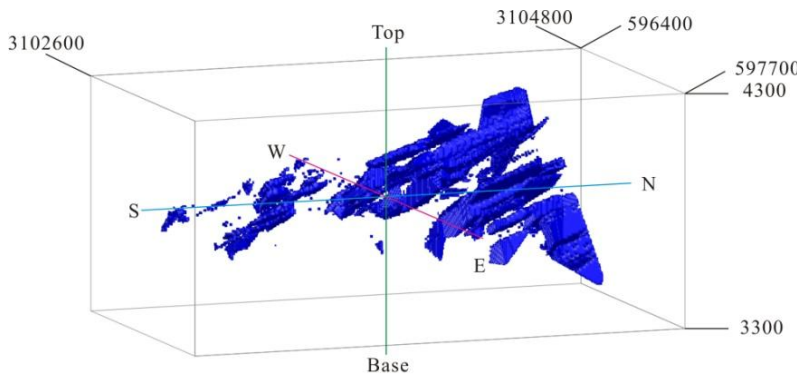
789

790 (b)



791

792 (c)

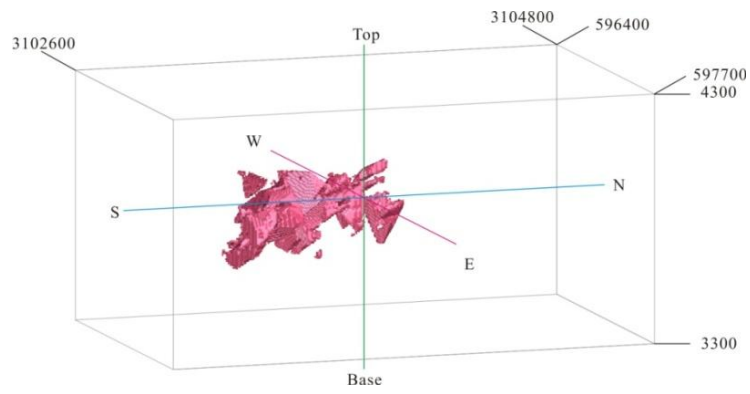


793

794

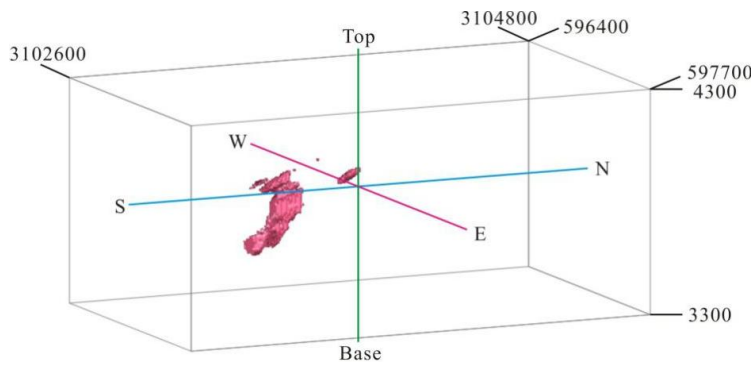
**Fig. 13.**

795 (a)



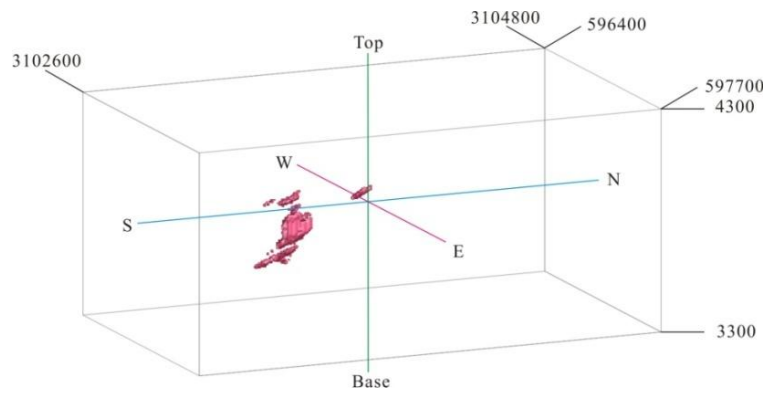
796

797 (b)



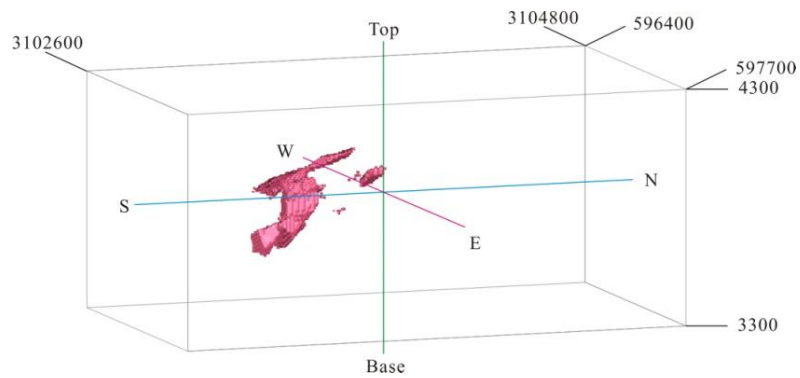
798

799 (c)



800

801 (d)



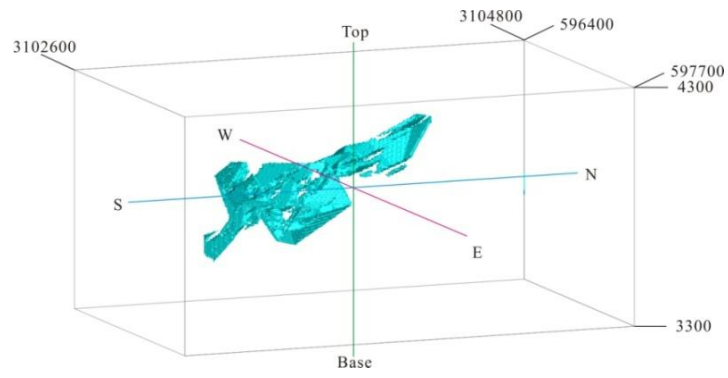
802

803

**Fig. 14.**

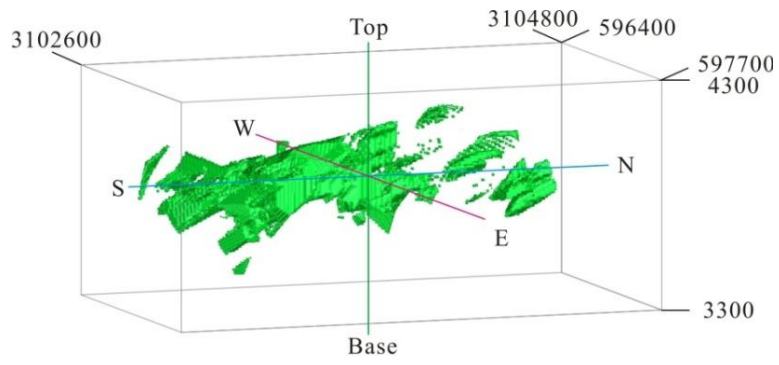


804 (a)



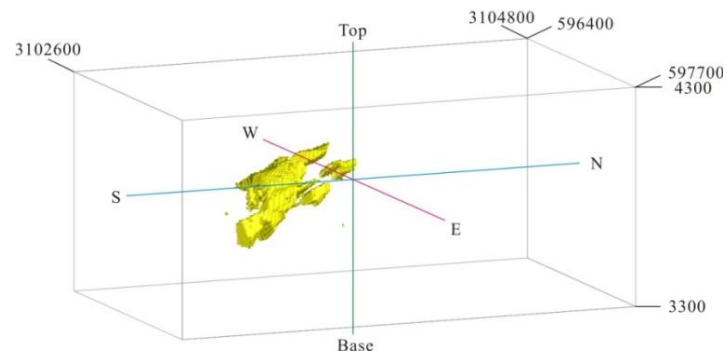
805

806 (b)



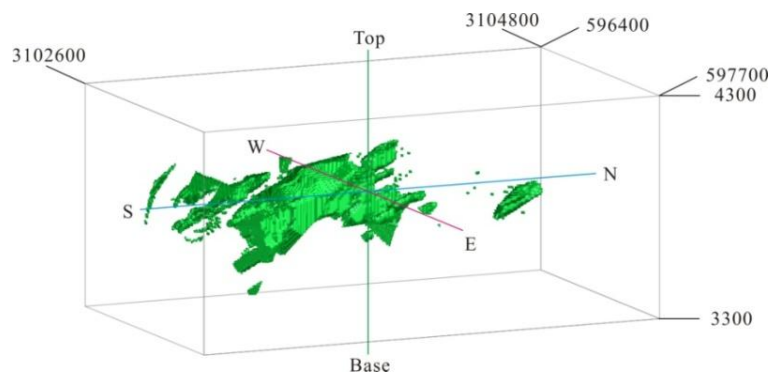
807

808 (c)



809

810 (d)



811

812

**Fig. 15.**

813

814  
815  
816  
817  
818  
819  
820  
821  
822  
823  
824  
825  
826  
827  
828  
829  
830  
831  
832  
833  
834  
835  
836  
837  
838  
839  
840  
841  
842  
843

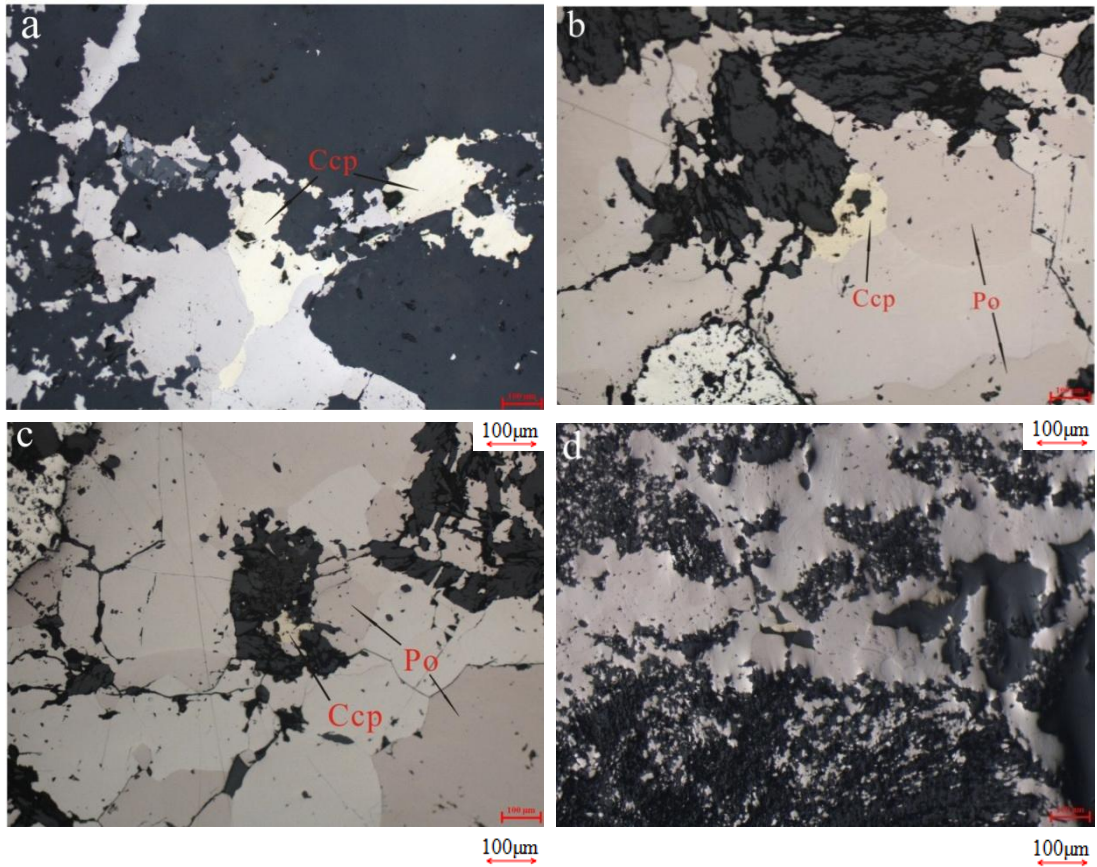


**Fig. 16.**

844 **Table 1**

Variables	Residual
Mean	0.000
Variance	0.016
Standard Deviation	0.127

845 **Table 2**

Mineralized zones	Thresholds(Cu%)	Range(Cu%)
Barren host rock and weakly mineralized		<0.28
Moderately mineralized	0.28	0.28-1.45
Highly mineralized	1.45	>1.45

846 **Table 3**

Mineralized zones	Thresholds(Cu%)	Range(Cu%)
Barren host rock		<0.25
Weakly mineralized	0.25	0.25–1.48
Moderately mineralized	1.48	1.48–1.88
Highly mineralized	1.88	>1.88

847 **Table 4**

Mineralized zones	PS threshold	Range of PS	Range(Cu%)
leached zone and barren host rock		<7.81	<0.23
hypogene zones	7.81	7.81-8.70	0.23-1.33
supergene enrichment zones	8.70	>8.70	>1.33

848 **Table 5**

		Geological model	
		Inside zone	Outside zone
Fractal model	Inside zone	True positive (A)	False positive (B)
	Outside zone	False negative (C)	True negative (D)
		Type I error = $C/(A+C)$	Type II error = $B/(B+D)$
		Overall accuracy = $(A+D)/(A+B+C+D)$	

849

850

851

852 **Table 6**

		Potassic alteration of geological model			
		Inside zones		Outside zones	
C–V fractal model of highly mineralized zones	Inside zones	A	2850	B	1360
	Outside zones	C	77927	D	76913
		T1E	0.96	T2E	0.02
		OA		0.50	
N–S fractal model of highly mineralized zones	Inside zones	A	3092	B	1570
	Outside zones	C	75025	D	75473
		T1E	0.96	T2E	0.02
		OA		0.51	
S–V fractal model of supergene enrichment zones	Inside zones	A	4431	B	2318
	Outside zones	C	72985	D	75726
		T1E	0.94	T2E	0.03
		OA		0.52	

853 **Table 7**

		Phyllic alteration of geological model			
		Inside zones		Outside zones	
C–V fractal model of moderately and weakly mineralized zones	Inside zones	A	36518	B	48027
	Outside zones	C	25461	D	69155
		T1E	0.41	T2E	0.40
		OA		0.59	
N–S fractal model of moderately mineralized zones	Inside zones	A	40080	B	44943
	Outside zones	C	26899	D	54239
		T1E	0.40	T2E	0.45
		OA		0.56	
S–V fractal model of the hypogene zones	Inside zones	A	35555	B	46943
	Outside zones	C	23955	D	48223
		T1E	0.40	T2E	0.49
		OA		0.54	

854 **Table 8**

Sample no.	Mineralized zones obtained by fractal models	Cu(%)
PL-B74	Weakly mineralized zones	0.41
PL-B62	Moderately mineralized zones	1.32
PL-B82	Highly mineralized zones	1.80

855